



## Experimental investigation and multiscale modeling of ultra-high-performance concrete panels subject to blast loading

B.D. Ellis <sup>a,\*</sup>, B.P. DiPaolo <sup>b</sup>, D.L. McDowell <sup>a,c</sup>, M. Zhou <sup>a,c</sup>

<sup>a</sup> Woodruff School of Mechanical Engineering, Georgia Institute of Technology, Atlanta, GA 30332-0405, USA

<sup>b</sup> U.S. Army Engineer Research and Development Center, 3909 Halls Ferry Road, Vicksburg, MS 39180, USA

<sup>c</sup> School of Materials Science and Engineering, Georgia Institute of Technology, Atlanta, GA 30332-0405, USA



### ARTICLE INFO

#### Article history:

Received 24 June 2013

Received in revised form

21 December 2013

Accepted 30 December 2013

Available online 14 February 2014

#### Keywords:

UHPC

Blast loading

Multiscale modeling

### ABSTRACT

Tailored cementitious materials, such as Ultra-High-Performance Concrete (UHPC), may significantly improve the blast resistance of structural panels. To understand and quantify the performance of UHPC panels subject to blast loading, four 1626- by 864- by 51-mm UHPC panels without steel rebar reinforcement were subjected to reflected impulse loads between 0.77 and 2.05 MPa-ms. The UHPC material was composed of a commercially available UHPC premix, high-range water reducing agent, 2% volume fraction of straight, smooth 14-mm-long by 0.185-mm-diameter fibers, and water. Experimental results determined that the UHPC panel fractured at a reflected impulse between 0.97 and 1.47 MPa-ms. These results were used to validate a multiscale model which accounts for structure and phenomena at two length scales: a multiple fiber length scale and a structural length scale. Within the multiscale model, a hand-shaking scheme conveys the energy barrier threshold and dissipated energy density from the model at the multiple fiber length scale to the model at the structural length scale. Together, the models at the two length scales account for energy dissipation through granular flow of the matrix, frictional pullout of the fibers, and friction between the interfaces. The simulated displacement and fracture patterns generated by the multiscale model are compared to experimental observations. This work is significant for three reasons: (1) new experimental data provide an upper and lower bound to the blast resistance of UHPC panels, (2) the multiscale model simulates the experimental results using readily available material properties and information regarding mesostructure attributes at two different length scales, and (3) by incorporating information from multiple length scales, the multiscale model can facilitate the design of UHPC materials to resist blast loading in ways not accessible using single length scale models.

© 2014 Elsevier Ltd. All rights reserved.

### 1. Introduction

To protect personnel and infrastructure, the dynamic response of materials and structures subject to blast loads must be understood. This understanding is especially important for new materials such as Ultra-High-Performance Concretes (UHPCs), which have been tailored at the micrometer and millimeter length scales to have compressive strengths exceeding 150 MPa [1] and enhanced fracture energies [2]. Here, a slab is assumed to be a representative structural element with which UHPC materials and their mesostructures will be characterized.

Since the introduction of UHPCs [3], results have been published for five experimental programs that subjected a total of 16 UHPC panels to blast loads at scaled distances ranging from 0.37 to 2.18 m/kg<sup>1/3</sup> [4]. Of the 16 panels, 13 panels were reinforced with steel rebar, and 3 panels were not reinforced. One of the three non-reinforced panels was 2- by 1- by 0.1-m in dimension and survived a reflected impulse of 1.62 MPa-ms [5]. The maximum and permanent centerline deflections were 13.2 and 4.1 mm, respectively. The two remaining non-reinforced UHPC panels were 3.5- by 1.3- by 0.1-m in dimension with one panel containing 2% volume fraction of fibers and the other panel containing 4% volume fraction of fibers [6]. After being subjected to a reflected impulse of 0.83 MPa-ms, the panels containing 2% and 4% fiber volume fractions permanently deflected 180 and 90 mm, respectively, at their mid-heights. Without testing until failure, the limited experimental

\* Corresponding author.

E-mail address: [bellis7@gatech.edu](mailto:bellis7@gatech.edu) (B.D. Ellis).

data provide only a lower limit to the critical load level; the upper bound remains to be established.

The responses of UHPC panels have been simulated by two different computational approaches. Wu et al. [5] used a layered single-degree-of-freedom model to predict the critical energy absorption capacity of UHPC panels with and without steel rebar reinforcement. This approach relies upon an a priori assumption of the elastic–plastic response of the panel [7], which defines a “shape function.” Hence, this approach is limited to elastic–plastic responses and cannot model fracture. In contrast to the single-degree-of-freedom approach, Zhou et al. [8] used a coupled damage-plasticity constitutive model that was pressure-sensitive and strain-rate dependent to determine the response of rebar-reinforced UHPC panels. Spall, defined as the ejection of mass on the surface opposite from that of the blast load impingement, was modeled by deleting elements with damage values exceeding 0.22 (on a scale from 0 to 1) during the first 0.5 ms after loading at strain rates greater than  $10 \text{ s}^{-1}$ . Although it accounts for spall, this approach underestimated the experimentally observed deflection by approximately 40%. Note that neither the layered single-degree-of-freedom model nor the damage-plasticity model included information from length scales smaller than the UHPC structure or steel rebar reinforcement levels; thus, neither approach is suitable for supporting materials design, i.e., tailoring the microstructure to achieve targeted responses or properties.

Gaps in the published literature motivated the objectives of the present study, namely, to experimentally determine the lower and upper bounds of the reflected impulse for a UHPC panel without rebar and to develop a multiscale model of UHPC panels based on the material properties and information regarding mesostructure attributes of the constituents.

## 2. Experimental setup

### 2.1. Materials

UHPC materials were made from Ductal® BS1000 Grey premix, Chryso® Fluid Primea 150 high-range water reducing agent, 2% volume fraction,  $V_{\text{fiber}}$ , of steel fibers, and water at a 0.19 nominal water-to-cementitious material ratio. The fibers were 14-mm long with 0.185-mm diameter circular cross-section and were measured to have a 2.16-GPa tensile strength, 210-GPa elastic stiffness, and 7.85-g/cm<sup>3</sup> mass density. The four constituents were mixed in a Nikko high-shear mixer according to the manufacturer's recommendation.

The mixed UHPC slurry was poured into four different rectangular cavities, each having dimensions of 1626-mm long by 864-mm wide by 50.4-mm deep. At the bottom of each cavity, two layers of Hardwire® 3 × 2-4-12-500 brass reinforcement [9] were placed at +45° and -45° from the direction of the 1626-mm length of the cavity. The panels were then cured at 22 °C under wet burlap for 24 h, followed by 2 days in a steam cabinet at 91 °C.

The mechanical properties of UHPC were obtained 14 days after pouring using three 101.6-mm-diameter by 203.2-mm-tall cylinders. The cylinders were poured from the same UHPC slurry and cured using the same protocol as the panels. Test results for the density,  $\rho_{\text{UHPC}}$ , and quasi-static unconfined compressive strength,  $f'_c$ , are in Table 1.

Fig. 1 shows a backscatter scanning electron microscope (SEM) image of a representative as-cured UHPC microstructure from Wang, Mattus, and Ren [10]. The black circle represents porosity, the white ellipses represent fibers, the dark grey represents quartz aggregate, and the regions between the previously listed components represent the paste. The magnified view at the right of Fig. 1 shows that the paste is composed of unhydrated clinker (white),

**Table 1**

Density and unconfined compressive strength for cylindrical specimens.

Sample ID	$\rho_{\text{UHPC}}$ (kg/m <sup>3</sup> )	$f'_c$ (MPa)
125-11DIP#1	2567	200
125-11DIP#2	2566	206
125-11DIP#3	2565	196
Mean	2566	201
Standard deviation	1.0	5.0

quartz powder (dark grey), cracks (black), and hydrated Calcium-Silicate-Hydrate (medium grey). Note that the SEM images were recorded in a vacuum, which implies that the visible cracks in the magnified view may be due to drying during the preparation of the specimen for SEM studies.

### 2.2. Blast load simulator (BLS)

Panels were tested at the U.S. Army Corps of Engineers (USACE) Engineer Research and Development Center (ERDC) Blast Load Simulator (BLS) located in Vicksburg, MS [11]. As shown in Fig. 2, the BLS is composed of a driver, expansion rings, straight rings, and the target vessel. After the UHPC panel is placed in the target fixture, the target vessel is connected to the straight rings. To initiate the test, a disk between the driver and expansion rings is ruptured, thus releasing the compressed air contained within the driver. The pressure wave travels through the expansion and straight rings before encountering the target located in the target vessel. The BLS produces planar waveforms with peak reflected pressures and impulses of 552 kPa and 11.0 MPa-ms, respectively.

Each UHPC panel was placed in the target fixture at the location indicated in Fig. 2. The target fixture consists of an insert and a cover as shown in Fig. 3a and b, respectively. The insert consists of two 203.2- by 152.4- by 12.7-mm structural steel tubes and two 50.8- by 50.8- by 6.35-mm structural tubes. The panel is placed in the insert with the Hardwire® reinforced surface adjacent to the 50.8- by 50.8- by 6.35-mm steel tubing. The cover keeps the panel in position before and during testing. The target fixture imposes conditions similar to, but not exactly the same as, “simply supported” boundary conditions.

Reflected pressure was recorded by six pressure transducers located at the positions shown as small yellow circles on the target fixture cover in Fig. 3b. Displacement of the distal face of one panel was recorded by an accelerometer and laser measurement system at the positions indicated in Fig. 3b. Video images of the distal faces of all panels were recorded at a rate of 1000 frames per second.

## 3. Multiscale modeling

The numerical simulations in this study were conducted based on a hierarchical multiscale modeling approach. The finest length scale, the multiple fiber length scale, simulates the fracture of the UHPC matrix and subsequent fiber pullout behavior. The coarsest length scale, the structural length scale, utilizes information from the multiple fiber length scale to simulate the behavior of the UHPC panel.

### 3.1. Multiple fiber length scale

A two-element Rigid-Body-Spring-Model (RBSM) was adopted at the multiple fiber length scale to define the traction-separation response of an interface bridged by fibers. The RBSM assumes that after the matrix at a given interface cracks, the entire load is carried by the fibers [12]. Here, the RBSM was introduced as part of

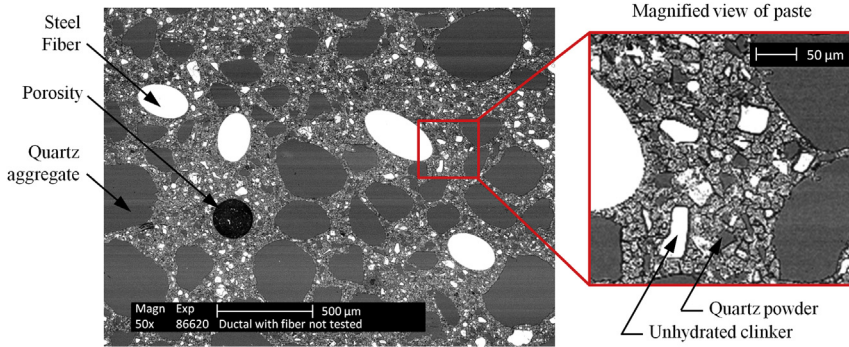


**Fig. 1.** Backscatter scanning electron microscope image of a representative as-cured UHPC microstructure [10].

a multiscale model, instead of a stand-alone model at the structural length scale (e.g., [13]).

As shown in Fig. 4, the RBSM model consists of two rigid elements, labeled 1 and 2, and a large number of fibers shaded in red that cross the  $x_1 = 0$  plane between the two rigid elements. Fibers are independently placed at pseudo-random positions and orientations within the model's domain until the 2% desired volume fraction is reached. Note that the fibers that do not cross the rigid element interface are not shown in Fig. 4. During deformation, rigid element 1 is restrained in all directions, while rigid element 2 is displaced by  $\delta$  in the  $x_1$  direction; all other translations and rotations of either rigid element are prohibited. By summing the force of each fiber, a homogenized traction-separation response can be calculated that accounts for fiber orientation, length, volume fraction, and force-end slip relations.

This model simplifies the multiple fiber length scale problem through several key assumptions. First, it is assumed that each fiber pulls out of the matrix and does not fracture. This assumption was based on physical experiments, after which fibers protruded from fractured surfaces on the recovered samples (cf. Section 4). It is further assumed that the matrix crack plane is predetermined, that the stress field around one fiber does not influence the stress field of other fibers [13], that all fibers uniformly displace during the imposed displacement  $\delta$ , each straight smooth fiber is strain-rate insensitive [14], and that after any fiber is removed from the matrix, the forces are instantly and uniformly distributed to the other fibers that cross the crack plane.

The model is decomposed into two parts: (1) pre-cracking tensile strength and (2) evolution of strength after matrix cracking. During the pre-cracking domain, the elastic stiffness of the composite is defined by a simple rule of mixtures approach, i.e.,

$$E_c = (1 - V_{\text{fiber}})E_m + \eta_1 \eta_\theta V_{\text{fiber}} E_f, \quad (1)$$

where  $E_c$  is the elastic stiffness of the two-phase composite,  $E_m$  is the elastic stiffness of the matrix,  $\eta_1$  is a parameter accounting for fiber embedded length defined as  $\eta_1 = 1 - \tanh(\beta L_{\text{fiber}}/2)/(\beta L_{\text{fiber}}/2)$ ,  $\beta$  is a parameter defined as  $\beta = \sqrt{2G_m/(E_f r^2 \ln(R/r))}$ ,  $G_m$  is the shear modulus of the matrix,  $E_f$  is the elastic stiffness of the fiber,  $r$

is the radius of the fiber,  $R$  is the mean radius of the matrix around one fiber,  $L_{\text{fiber}}$  is the total length of the fiber,  $\eta_\theta$  is a parameter associated with orientation of fiber defined as  $\eta_\theta = (1/N_f) \sum_{i=1}^{N_f} \cos^4 \theta_i$ ,  $N_f$  is the total number of fibers that cross the crack plane, and  $\theta_i$  is the inclination angle of the  $i$ th fiber between the fiber's direction and that of the direction of displacement (i.e.,  $x_1$ ). At a displacement of  $L_{\text{matrix}} \varepsilon_{\text{mu}}/2$ , the pre-cracking strength is  $f_{t,\text{pre}} = E_c \varepsilon_{\text{mu}}$ , where  $\varepsilon_{\text{mu}}$  is the fracture strain of the matrix without fibers.

After cracking of the matrix, the evolution of tensile strength,  $f_t(\delta)$ , is calculated by summing the pullout resistance of each fiber that crosses the predefined crack plane, i.e.,  $f_t(\delta) = \sum_{i=1}^{N_f} f_{i\theta}(L_e, \delta)$ , where  $f_{i\theta}$  is the pullout resistance of the  $i$ th fiber accounting for the inclination angle, and  $L_e$  is the minimum embedded length in a Euclidian sense. The relation between  $f_{i\theta}$  and the pullout resistance of the  $i$ th fiber oriented parallel to the pullout direction,  $f_i$ , is assumed to be

$$f_{i\theta}(L_e, \delta) = \begin{cases} f_i(L_e, \delta)/\cos(\theta_i) & \text{for } -45^\circ \leq \theta_i \leq 45^\circ \\ f_i(L_e, \delta)/\cos(45^\circ) & \text{for } |\theta_i| \geq 45^\circ \end{cases} \quad (2)$$

The form of Eq. (2) is based on experimental work of Li et al. [15], who measured the pullout force of straight, smooth fibers at inclination angles between 0° and 60°.

The pullout force  $f_i$  can be determined by experiments, analytical models, or numerical techniques. Here, an analytical fiber debonding model was utilized that assumes the fiber slips out of the matrix and does not rupture. Resistance to slipping is characterized by the interfacial shear strength,  $\tau_s$ , which represents the

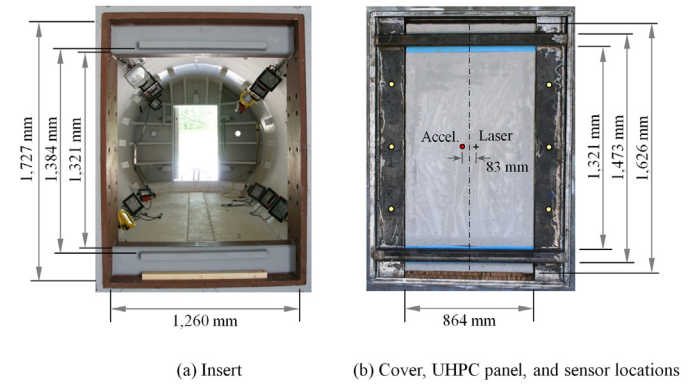


**Fig. 3.** Target fixture as viewed from section A–A (cf. Fig. 2) showing the (a) target fixture insert and (b) target fixture cover, proximal face of UHPC panel, and sensor locations.

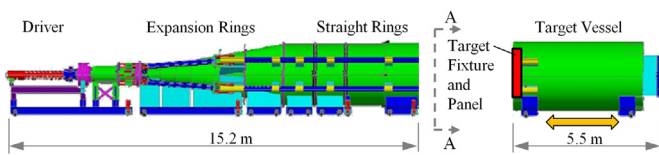


**Fig. 2.** Schematic of blast load simulator (BLS).

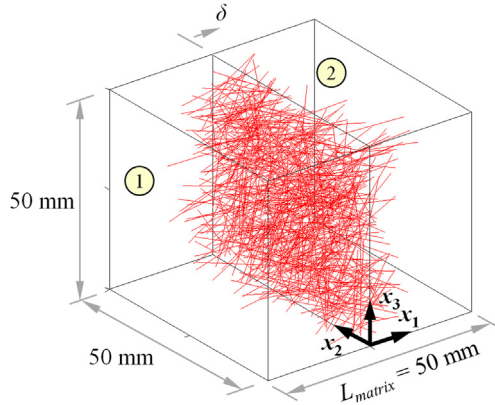


**Fig. 4.** Sample instantiation of the Rigid-Body-Spring-Model (RBSM) at the multiple fiber length scale with  $V_{\text{fiber}} = 2\%$ , 14-mm fiber length, and 0.185-mm fiber diameter.

chemical bonding between the fiber and the matrix, and the frictional shear strength,  $\tau_i$ , which represents the mechanical resistance to the fiber slipping. By assuming that  $\tau_s$  and  $\tau_i$  are equal, Gopalaratnam and Shah [16] showed that  $f_i$  increases linearly to the maximum pullout force

$$f_{\max} = \max \left( \frac{\frac{2\pi r \tau_s}{\beta} \sinh(\beta m L_e / 2) + \pi r L_e \tau_i (1 - m) \cosh(\beta m L_e / 2)}{(1 - \alpha) \cosh(\beta m L_e / 2) + \alpha} \right), \quad (3)$$

and then decreases linearly to zero at  $\delta = L_e$ . In Eq. (3),  $r$  and  $\beta$  were previously defined,  $m$  is a monotonically increasing parameter that ranges from zero for an undamaged fiber–matrix interface to one for a completely damaged fiber–matrix interface, and  $\alpha = A_f E_f / (A_m E_m)$  is a non-dimensional parameter relating the area of the fiber,  $A_f$ , and the elastic modulus of the fiber to the area of the matrix,  $A_m$ , and the elastic modulus of the matrix. An approximate solution to Eq. (3) can be found by assuming that  $(1 - \alpha) \cosh(\beta m L_e / 2) \gg \alpha$ , which results in  $f_{\max}$  to be found at  $m_{cr} \approx 2a \cosh \sqrt{\tau_s / \tau_i} / \beta L_e$ . Material parameters for the matrix were assigned as  $\nu_m = 0.2$  and  $\varepsilon_{mu} = 0.20 \times 10^{-3}$ , representative of a matrix with 200-MPa unconfined compressive strength,  $f_m$ . The elastic stiffness,  $E_m$ , is calculated using the empirical relation

$$E_m = 2.15 \times 10^4 (f_m / 10)^{1/3}, \quad (4)$$

which is a fit to the prediction of the CEP-FIP Model 1990 [17]. In the above relation,  $f_m$  and  $E_m$  are specified in MPa. Equation (4) is valid for normal weight concretes with quartz aggregates and  $f_c \leq 80$  MPa at 28 days. Even though  $f_m = 200$  MPa is outside the recommended limit, the calculated 58.4-GPa elastic stiffness is within the manufacturer's recommended range of 58–62 GPa [18]. Values of the interfacial shear strength,  $\tau_i$ , for uncoated straight, smooth fibers were experimentally measured to be 5 [19], 4.8–5.5 [20], 6–8 [21], and 10 MPa [22]. Here, it is assumed that  $\tau_i = \tau_s = 6$  MPa.

### 3.1.1. Homogenization at the multiple fiber length scale

The two-element RBSM is homogenized to the structural length scale through a hand-shaking scheme. The scheme uses four variables – mean tensile strength, standard deviation of the tensile strength, mean dissipated energy density, and standard deviation of the dissipated energy density – generated from 100 realizations at the multiple fiber length scale to populate cohesive properties in the normal and tangent directions at the structural length scale. In this manner, the homogenization scheme ensures that the energy barrier to fracture, i.e., the maximum tensile stress, and the dissipated energy are consistent between length scales.

Fig. 5a shows the tensile stress versus displacement, in which the dissipated energy density is the integral of tensile stress over the displacement  $\delta$ ; Figs. 5b and 5c show histograms of the maximum tensile strength and the dissipated energy density with Gaussian distribution function overlaid on the histogram.

### 3.2. Structural length scale

As shown in Fig. 6, the model at the structural length scale is implemented in three dimensions and consists of a UHPC panel shaded in red constrained by steel restraints shaded in gray. The face of the panel in Fig. 6 is denoted the proximal face; the face not shown is denoted the distal face. The panel consists of bulk elements and zero-thickness cohesive elements, which connect two adjacent bulk elements together. Bulk elements dictate the compressive properties of the panel and are modeled with the extended Drucker–Prager constitutive model described in Section 3.2.1. Cohesive elements dictate the tensile response and are described by the constitutive model in Section 3.2.2. As indicated in Fig. 6, a Gaussian distribution is assumed for the critical tractions and the work of separation of the cohesive elements. The restraints are modeled with a rate-sensitive Johnson–Cook constitutive model described in Section 3.2.3. Friction is modeled with a rate- and pressure-independent, isotropic Coulomb friction law described in Section 3.2.4. The default penalty contact algorithm

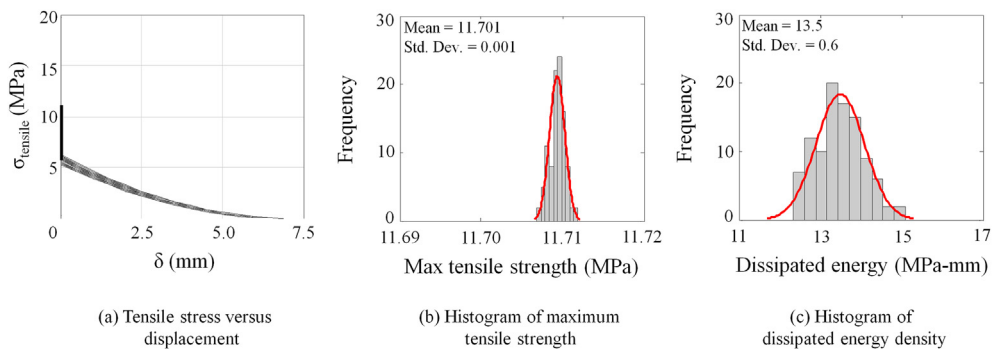


**Fig. 5.** Stochastic variation of (a) tensile stress versus displacement, which leads to mean and standard deviation values of (b) maximum tensile strength and (c) dissipated energy density.

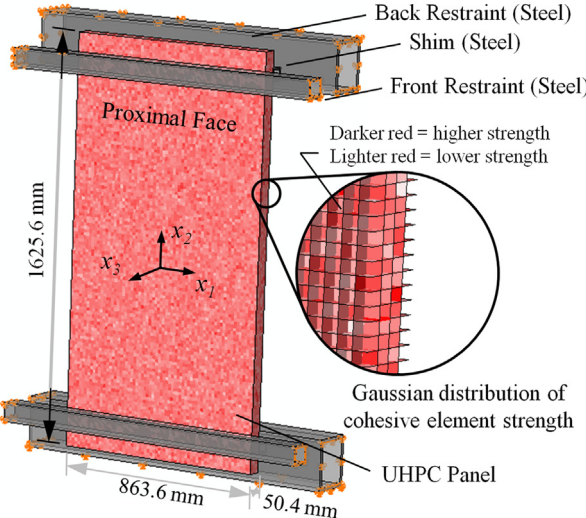


**Fig. 6.** Model at the structural length scale showing the proximal face and restraints.

within ABAQUS/Explicit v6.10 [23] is used to enforce contact constraints between elements.

The panel is located between the front restraints and shims attached to the back restraints such that there are neither gaps nor compressive tractions between the panel and the restraints. The shims and restraints used in the model match the restraints in the physical experiment except that internal and external radii are not modeled.

Prior to loading, the nodes on the positive and negative  $x_1$  faces of the four restraints are prevented from translating or rotating. Two additional boundary conditions are defined for the back restraints. First, the nodes on the positive  $x_2$  face on the top back restraint are prevented from translating and rotating. Second, the nodes on the negative  $x_2$  face on the bottom back restraint are prevented from translating and rotating. After applying boundary conditions to the four restraints, the proximal face of the panel is loaded by a time-dependent pressure in the negative  $x_3$  direction. A pressure of  $p_{\max}$  is applied at 0 ms and linearly decreases to 0 Pa at 15 ms, the time when video images indicate complete fracture of the panel. The applied specific impulse is  $I = (15 \text{ ms}/2)p_{\max}$ .

### 3.2.1. Drucker–Prager constitutive model

The bulk elements in the UHPC panel are represented by an extended Drucker–Prager constitutive relation included in ABAQUS/Explicit v6.10 [23]. The extended Drucker–Prager constitutive relation assumes the yield condition

$$F = t - p \tan(\beta) - d \leq 0, \quad (5)$$

where  $t = (q/2)[1 + 1/K - (1 - 1/K)(r/q)^3]$ . Here,  $p$  is the pressure defined by  $p = -1/3\sigma : \mathbf{I}$ ,  $\sigma$  is the Cauchy stress,  $\mathbf{I}$  is the 2nd rank identity tensor,  $\beta$  is the internal friction angle in the meridional stress plane,  $d$  is the cohesion of the material under pure shear,  $q$  is the Mises equivalent stress defined by  $q = \sqrt{(3/2)(\mathbf{S} : \mathbf{S})}$ ,  $\mathbf{S}$  is the deviatoric stress tensor defined as  $\mathbf{S} = \sigma + p\mathbf{I}$ ,  $K$  is the ratio between the yield stress in triaxial tension and the yield stress in triaxial compression and must be in the range  $0.778 \leq K \leq 1.0$ , and  $r$  is the third invariant of the deviatoric stress defined by  $r = ((9/2)\mathbf{S} : \mathbf{S})^{1/3}$ . Setting  $K = 1$  allows the original Drucker–Prager [24] yield condition to be recovered due to the lack of

dependence on the third invariant of deviatoric stress. The von Mises yield condition is recovered when  $K = 1$  and  $\beta = 0$ .

When the yield condition is satisfied (i.e.,  $F = 0$ ), a non-associative material yields according to the flow rule

$$\mathbf{D}^p = \frac{\dot{\varepsilon}^p}{c} \frac{\partial G}{\partial \sigma} \quad (6)$$

where  $\mathbf{D}^p$  is the plastic part of the rate of deformation tensor,  $\dot{\varepsilon}^p$  is the equivalent plastic strain rate defined by  $\dot{\varepsilon}^p = \sqrt{(2/3)\mathbf{D}^p : \mathbf{D}^p}$ ,  $c$  is a constant defined by  $c = 1 - 1/3\tan(\psi)$ ,  $G$  is the flow potential defined by  $G = t - p\tan(\psi)$ , and  $\psi$  is the dilation angle.

The mass density,  $\rho$ , and unconfined yield strength,  $f'_c$ , were specified as  $2.57 \text{ g/cm}^3$  and  $200 \text{ MPa}$ , respectively. The remaining constants for the constitutive model were obtained from the literature. The ratio of the yield stress in triaxial tension to the yield stress in triaxial compression, the internal friction angle, and the dilation angle were determined by Park, Xia, and Zhou [25] to be  $K = 0.8$ ,  $\beta = 28^\circ$ , and  $\psi = 20^\circ$ , respectively. The elastic stiffness,  $E_c$ , is calculated using Eq. (1). Possible softening of the matrix during large deformation and strain-rate sensitivity are not considered.

### 3.2.2. Bilinear traction-separation

Interfacial debonding between bulk elements is modelled using zero-thickness cohesive elements and a strain-rate sensitive traction-separation constitutive model implemented via a custom VUMAT subroutine called by ABAQUS/Explicit. If the strain rate,  $\dot{\varepsilon}$ , is equal to a quasi-static strain rate, the model assumes the bilinear response shown in Fig. 7, where  $T$  is the traction,  $\delta$  is the separation,  $K$  is the stiffness, and  $G^c$  is the work of separation defined as the integral of traction from zero separation to the separation at complete failure,  $\delta^f$ . Subscripts  $n$ ,  $s$ , and  $t$  indicate the normal and two tangential directions, respectively.

The strain rate of each element at each time interval is calculated by  $\dot{\varepsilon} = \max(d\delta_{n,s,t}/(dt_{\text{elem}}))$ , where  $d\delta_{n,s,t}$  is the incremental separation in the  $n$ ,  $s$ , and  $t$  directions,  $dt$  is the time step, and  $L_{\text{elem}}$  is the characteristic element size. The dynamic tensile strength,  $T_{n,s,t}^e$ , is defined as  $T_{n,s,t}^e = TDIF \times T_{n,s,t}^o$ , where the tensile dynamic inflation factor (from Zhou et al. [8]) is expressed as

$$TDIF = \begin{cases} 1 & \text{for } \dot{\varepsilon} \leq 10^{-4} \text{ s}^{-1} \\ 2.06 + 0.26 \log_{10} \dot{\varepsilon} & \text{for } 10^{-4} \text{ s}^{-1} < \dot{\varepsilon} \leq 1 \text{ s}^{-1} \\ 2.06 + 2.0 \log_{10} \dot{\varepsilon} & \text{for } 1 \text{ s}^{-1} < \dot{\varepsilon} \leq 10^3 \text{ s}^{-1} \end{cases} \quad (7)$$

For  $\dot{\varepsilon} > 10^3 \text{ s}^{-1}$ , a conservative estimate of  $\dot{\varepsilon} = 10^3 \text{ s}^{-1}$  is assumed. As suggested by Kim et al. [14], the work of extracting straight, smooth fibers from a cementitious matrix is relatively rate insensitive; hence, it was assumed that the work or separation is invariant with respect to strain-rate.

The initial linear-elastic portion in Fig. 7 is decoupled in the normal and tangential directions (i.e.,  $T_i = K_i \delta_i$  where  $i = n, s, t$  without summation implied, and  $K_i = 200 \text{ GPa}$  is the stiffness in the  $i^{\text{th}}$  direction). Damage initiation (peak traction in Fig. 7) leads to coupling between the normal and tangential directions and is governed by the quadratic initiation criterion

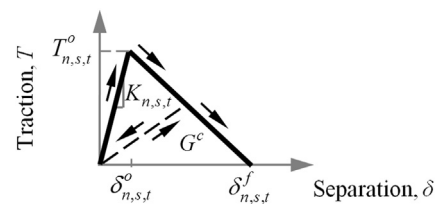


**Fig. 7.** Traction-separation constitutive law for the fiber–matrix interface.

$(\langle T_n \rangle / T_n^{\dot{\varepsilon}})^2 + (T_s / T_s^{\dot{\varepsilon}})^2 + (T_t / T_t^{\dot{\varepsilon}})^2 = 1$ , where the Macaulay brackets are defined by  $\langle x \rangle = 1/2(|x| + x)$ . Damage evolution is calculated by  $d = \max(\delta_i^f(\delta_i^{\max} - \delta_i^o)/(\delta_i^{\max}(\delta_i^f - \delta_i^o)))$ , where  $i = n,s,t$  without summation implied, and  $\delta^{\max}$  is the maximum separation during the loading history [23]. The material parameters are listed in Table 2.

### 3.2.3. Johnson–Cook plasticity model

The restraints are assumed to be elastic–viscoplastic. Yielding of the restraint is assumed to follow the Von Mises yield criterion in the form

$$F(\sigma, \dot{\varepsilon}^{pl}, \dot{\varepsilon}^{pl}) = \mathbf{S} : \mathbf{S}/2 - (\sigma^0(\dot{\varepsilon}^{pl}, \dot{\varepsilon}^{pl}))^2/3 = 0, \quad (8)$$

where  $\dot{\varepsilon}^{pl}$  and  $\dot{\varepsilon}^{pl}$  are the equivalent plastic strain and equivalent plastic strain rate, respectively. The Johnson–Cook model [26] defines the current yield stress as

$$\sigma^0(\dot{\varepsilon}^{pl}, \dot{\varepsilon}^{pl}) = [A + B(\dot{\varepsilon}^{pl})^n][1 + C \log_{10}(\dot{\varepsilon}^{pl}/\dot{\varepsilon}_0)], \quad (9)$$

where  $A$ ,  $B$ ,  $n$ , and  $C$  are material parameters, and  $\dot{\varepsilon}_0$  is a reference strain rate. In Eq. (9), the temperature effects of the Johnson–Cook model are ignored; thus, it is assumed that reflected pressures cause inappreciable heating in the constraints during loading. Because the inelastic flow is assumed to be associative, the evolution equation for plastic strain is given by

$$\dot{\varepsilon}^{pl} = \lambda \frac{\partial F}{\partial \sigma}, \quad (10)$$

where  $\lambda$  is the plastic multiplier obtained from the consistency condition  $dF = 0$  during plastic flow.

Table 3 lists the mass density,  $\rho_f$ , Young's modulus,  $E_f$ , Poisson's ratio,  $\nu_f$ , and parameters in the Johnson–Cook model ( $A$ ,  $B$ ,  $n$ ,  $C$ , and  $\dot{\varepsilon}_0$ ) for the restraint material, representing a typical 4340 steel [26].

### 3.2.4. Friction model

The friction model used is the rate-independent, isotropic Coulomb friction law. In this model, relative motion between two surfaces is allowed when the equivalent shear stress  $\tau_{eq} = \sqrt{\tau_1^2 + \tau_2^2}$  reaches or exceeds the critical stress  $\tau_{crit} = \mu p_{contact}$ , where  $\tau_1$  and  $\tau_2$  are mutually orthogonal shear stresses at the interface,  $\mu$  is the coefficient of friction, and  $p_{contact}$  is the normal contact pressure between the two surfaces. Because the model is assumed to be isotropic, the magnitudes of the shearing rates  $\dot{\gamma}_1 = \sqrt{\dot{\gamma}_1^2 + \dot{\gamma}_2^2}\tau_1/\tau_{eq}$  and  $\dot{\gamma}_2 = \sqrt{\dot{\gamma}_1^2 + \dot{\gamma}_2^2}\tau_2/\tau_{eq}$  are proportional to the shear stresses  $\tau_1$  and  $\tau_2$ .

The coefficient of Coulomb friction is determined from the experiments of Baltay and Gjelsvik [27], who found that the coefficient of friction between steel and concrete depends on the surface finish of the steel. For machined surfaces, the mean coefficient of friction was measured over the range of normal pressures from 13.8 kPa to 55 MPa. Although Baltay and Gjelsvik [27] assigned a mean value of 0.47, the data for machined steel surfaces indicate a parabolic response with the maximum value of  $\mu = 0.58$  for a

Table 3

Material parameters for 4340 steel (restraint).

Material	$\rho_f$ (g/cm <sup>3</sup> )	$E_f$ (GPa)	$\nu_f$	$A$ (MPa)	$B$ (MPa)	$n$	$C$	$\dot{\varepsilon}_0$ (s <sup>-1</sup> )
4340	7.85	200	0.3	792	510	0.26	0.014	1

normal stress of 3.4 MPa and a minimum value of  $\mu = 0.35$  for  $p_{contact} \leq 3.4$  MPa and  $p_{contact} \geq 55$  MPa. For steel surfaces with mill scale, Baltay and Gjelsvik [27] reported that the coefficient of friction is 0.2 for  $p_{contact} = 10$  kPa and increases to 0.53 for  $p_{contact} = 34.5$  MPa. In this work, a pressure-independent coefficient was assumed for simplicity with a friction value of 0.45.

### 3.2.5. Meshing and numerical algorithm

Bulk elements in both the panel and the four restraints were 8-node hexahedral elements with linear interpolation functions. The elements in both the panel and the restraints had 12.7- and 16-mm characteristic element sizes, respectively. The cohesive elements between the panel's bulk elements were zero thickness 8-node hexahedral elements. The width and length of the cohesive elements match the 12.7-mm characteristic element size of the bulk elements in the panel. Each instantiation consists of approximately 45,000 bulk and 100,000 cohesive elements. The commercial code ABAQUS/Explicit v6.10-1 was used to solve the model on 48 parallel AMD 2350QC processing cores in a UNIX cluster. Boundary conditions and simulated loading follow those described in Section 3.2. For the 40-ms simulation time considered, processing times varied from 20 to 30 h depending on the severity of contact and damage.

## 4. Results

Four physical panels were subjected to reflected impulses from 0.81 to 2.05 MPa-ms. Three of the panels were intact and imperforated at time of impulse loading; one panel was intentionally perforated prior to being impulsively loaded. Panel 1 was fitted with an accelerometer and laser displacement system, whereas the other three panels (i.e., Panels 2, 3, and 4) were not. For the four panels tested, fracture created negligible particle debris and generated fracture surfaces containing protruding fibers.

Panels 1, 2, and 3 were intact, imperforated at the time of impulse loading. Panel 1 fractured when exposed to a reflected impulse of 2.05 MPa-ms. Panel 2 fractured when exposed to a reflected impulse of 1.70 MPa-ms. Panel 3 survived two tests – the first at a reflected impulse of 0.81 MPa-ms, and the second at a reflected impulse of 0.97 MPa-ms – before fracturing during a third test at a 1.47-MPa-ms impulse. Panel 3's three tests were separated in time such that visual inspection and permanent deflections could be measured between tests. After surviving the first test at a 0.81-MPa-ms impulse, visual inspection by an unaided eye found no damage to Panel 3's proximal and distal faces. However, the 0.81-Mpa-ms impulsive load caused Panel 3's vertical centerline to permanently deflect approximately 10 mm in the loading direction (i.e., displaced in the negative  $x_3$  direction). After surviving the second test at a 0.97-MPa-ms impulse, visual inspection found very little damage to Panel 3's proximal and distal faces. Permanent deflection of the vertical centerline increased to approximately 19 mm in the loading direction (i.e., displaced in the negative  $x_3$  direction). From the experiments, the critical impulse that caused an initially intact, imperforated panel to fracture was between 0.97 and 1.47 MPa-ms. All three panels fractured at three locations: near bottom support, slightly below the mid-height of the panel, and near the top support.

Prior to testing, Panel 4 was intentionally perforated with five holes, each approximately 13 mm in diameter. The first hole was

Table 2

Cohesive element material properties.

$K_{n,s,t}$ (GPa)	$T_{n,s,t}^0$ (MPa)		$G_{n,s,t}^c$ (kJ/m <sup>2</sup> )	
	Mean	Std. dev.	Mean	Std. dev.
200	11.7	0.0	13.5	0.6

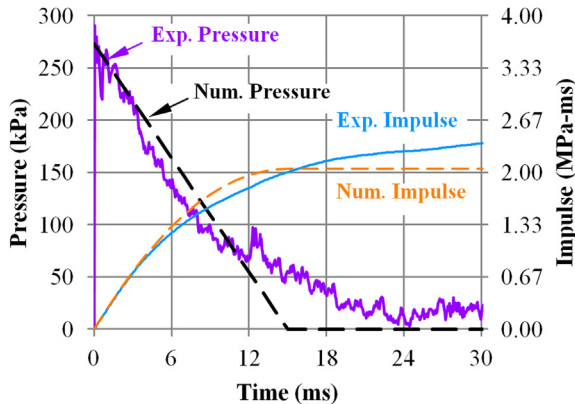


**Fig. 8.** Idealized pressure and impulse compared to the experimentally observed pressure and impulse for validating multiscale model.

located at the center of the panel; the remaining four holes were located 203 mm from the center of the panel in the positive and negative  $x_1$  and  $x_2$  directions (cf. Fig. 6). After being loaded with a 0.97-MPa-ms impulse, Panel 4 fractured at two locations: near the bottom support, and through the 3 holes near the mid-height of the panel. Clearly the perforations reduced the energy threshold required to initiate fracture at the mid-height of the panel. The reduced energy threshold further reduced the panels ability to dissipate energy via fracture because only two fracture surfaces were created.

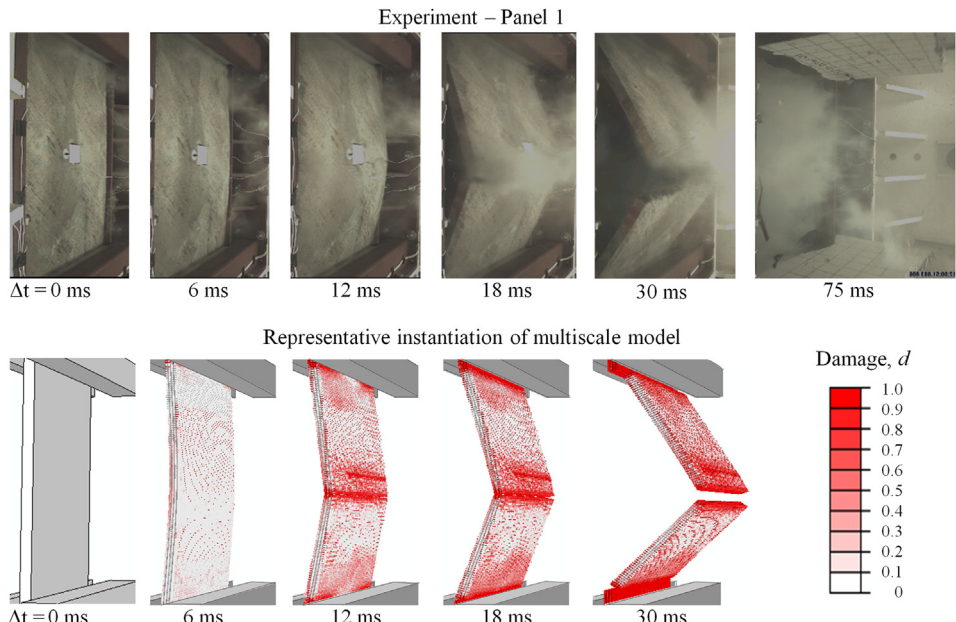
Validation of the multiscale model was based on five instantiations of the numerical model at the structural length scale satisfying three criteria: (1) critical impulse to fracture the panel, which created two or more separate sections of the panel; (2) qualitative comparison of fracture patterns; and (3) displacement at the mid-height of the panel. The critical specific impulses calculated for all five instantiations were between a 0.97-MPa-ms

lower bound and a 1.21-MPa-ms upper bound, which is within the experimentally determined 0.97-MPa-ms lower bound and 1.47-MPa-ms upper bound.

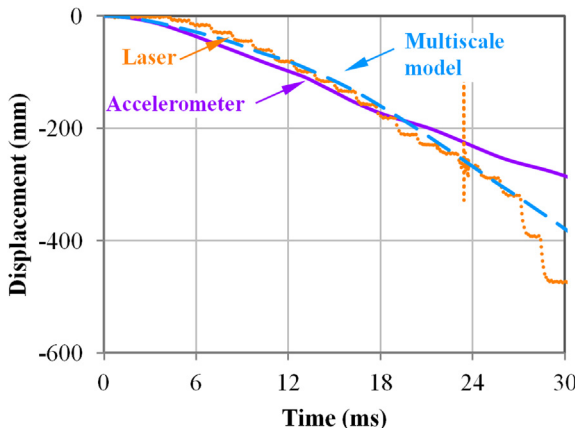
The remaining two validation criteria were based on experimental results with an experimentally observed impulse of 2.05 MPa-ms after 15 ms, the time at which a through crack was evident. Fig. 8 shows a comparison between the numerically applied pressure shown as a black dashed line and the experimentally measured pressure shown as a solid purple line. The resulting experimentally observed and numerically applied impulses are shown as solid blue and dashed orange lines, respectively.

Fig. 9 shows the deformation and fracture patterns of Panel 1, which was subjected to a 2.05-MPa-ms impulse, and a representative instantiation of the multiscale model subjected to the same impulse. At 6 ms, the experiment and the simulation indicate parabolic deformation; moreover, the simulation exhibits distributed cracking. At 12 ms, the distributed cracks in the simulation coalesced into two prevailing cracks near the panel's mid-height. Images of the experimental panel indicate similar phenomena with the distributed cracking coalescing into the characteristic mid-height fracture. Subsequently, the simulated panel fractures at two additional locations near the top and bottom restraints. Because the video was obtained from the distal face, it is assumed that the fractures near the top and bottom restraints occurred after the mid-height fracture.

The last criterion for model validation was the displacement of the center of the panel as a function of time, as shown in Fig. 10. For times less than 18 ms, the simulation under-predicts the displacement measured by the accelerometer by a maximum of 23%. Several possible reasons for the error include the assumed strain of the matrix at failure,  $\epsilon_{mu}$ , the assumed strain-rate tensile dynamic inflation factor, and the exclusion of fluid-structure interactions. For times greater than 18 ms, accelerometer data and video images indicate that the numerical simulation over-predicts displacements. One possible reason for the over-prediction is that the multiscale model does not consider the two layers of Hardwire®



**Fig. 9.** Images of Panel 1 and one instantiation of the multiscale model of a UHPC panel subjected to a 2.05-MPa-ms reflected impulse. The instantiation exhibits distributed cracking at 6 ms before crack coalescence and growth at 12 ms. Both the experiments and numerical simulations show three areas of characteristic fracture – one at the lower restraint, one at the mid-height, and one at the top restraint.



**Fig. 10.** Comparison of displacement of the center of the panel in the  $x_3$  direction (cf. Fig. 6) measured by accelerometer and laser interferometer measurement systems and the displacement predicted by a representative instantiation of the multiscale model ( $I = 2.05 \text{ MPa-ms}$ ).

brass reinforcement located on the distal face of the physical panels. However, the mid-height crack coalescence at 12 ms suggests that the exclusion of the distal face mesh did not influence the bounds of the calculated critical specific impulses. Displacement data does not exist for lower impulse experiments; thus, only one impulse level is used for model validation.

After validation, the multiscale model was utilized to predict the damage initiation impulse at which the panel accumulated less than 1% total damage. Here, the total damage is defined as the sum of damage of all cohesive elements divided by the total number of cohesive elements. As shown by the evolution of total damage for impulses between 0.24- and 2.05-MPa-ms in Fig. 11, an impulse of 0.24-MPa-ms produced a total damage of less than 1% for the material parameters considered. The determination of the damage initiation impulse allows panels to be quickly assessed after subjected to a given impulse load.

A final result of this investigation was a parametric study determining the influence of mean values of  $T_{n,s,t}^o$  and  $G_{n,s,t}^c$  on the critical specific impulse required to completely fracture the simulated panel. Results of the parametric study are shown in Fig. 12 with tensile strengths of 14.7, 20, and 40 MPa shown as blue circles, purple triangles, and orange squares, respectively. The validation point using the material properties from Table 2 is shown as

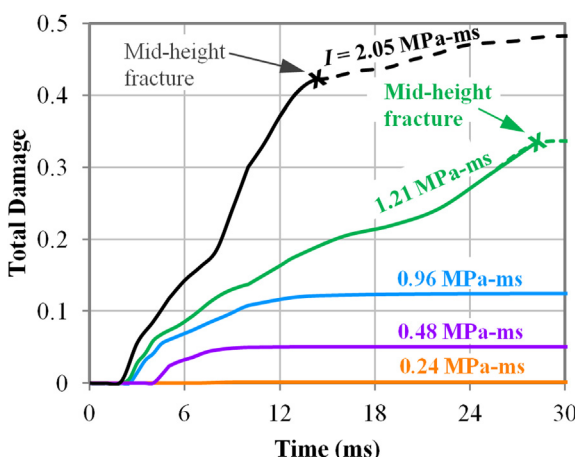


**Fig. 11.** Total damage predicted for simulated UHPC panel with an 11.7-MPa mean  $T_{n,s,t}^o$  and 13.5- $\text{kJ}/\text{m}^2$  mean  $G_{n,s,t}^c$  for impulses between 0.24- and 2.05-MPa-ms.

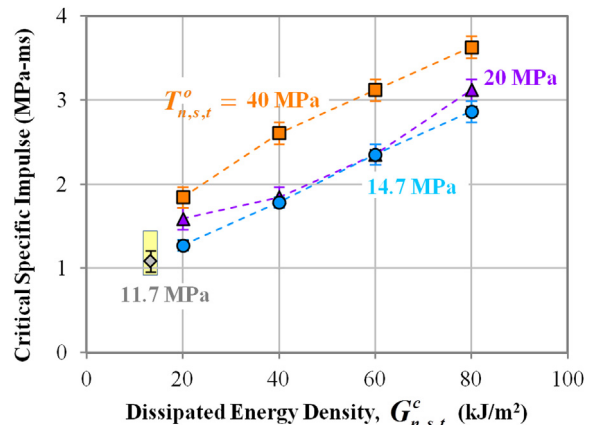


**Fig. 12.** Calculated critical specific impulse required to completely fracture the simulated UHPC panel with dissipated energy densities between 20 and 80  $\text{kJ}/\text{m}^2$  and tensile strengths of 14.7, 20, and 40 MPa.

a gray diamond within the experimentally determined range of 0.97- to 1.47-MPa-ms, which is indicated by a yellow rectangle. As expected, the critical specific impulse increased as the dissipated energy density at the interface increased and as the maximum tensile strength increased. For a dissipated energy density of 20  $\text{kJ}/\text{m}^2$ , doubling the tensile strength from 20 to 40 MPa increases the critical specific impulse by only 16%. In comparison, doubling the dissipated energy density from 20 to 40  $\text{kJ}/\text{m}^2$  increases the critical specific impulse by 40% for a 14.7-MPa tensile strength. These results indicate that increasing the dissipated energy density, e.g., increasing the fiber content or changing the fiber geometry, offers the most effective avenue for improving the critical specific impulse.

An unexpected result is that the critical specific impulse is very similar for tensile strength values of 14.7 and 20 MPa at dissipated energy density values of 40 and 60  $\text{kJ}/\text{m}^2$ . Specifically, for simulated UHPC panels with a tensile strength of 20 MPa and dissipated energy density values of 40 and 60  $\text{kJ}/\text{m}^2$ , cracks coalesce more rapidly than other simulations. This result indicates that these combinations of tensile strength and dissipated energy densities lead to a “brittle” structural response.

## 5. Conclusions

Four Ultra-High-Performance Concrete (UHPC) panels of dimension 1626 by 864 by 50 mm were subjected to planar waveforms with specific impulses between 0.77 and 2.05 MPa-ms within a test apparatus at ERDC. The UHPC panels were constructed from commercially available materials without steel rebar reinforcement. Results of these experiments indicated that the critical specific impulse for the UHPC panels was bounded between 0.97 and 1.47 MPa-ms. During fracture, all four UHPC panels generated negligible debris and left protruding fibers on the fractured surfaces.

The physical experiments provided a basis for a hierarchical multiscale model consisting of two length scales – a multiple fiber length scale and a structural panel length scale. These length scales were bridged by a hand-shaking scheme that conveyed four relevant quantities – mean tensile strength, standard deviation of the tensile strength, mean dissipated energy density, and standard deviation of the dissipated energy density – from the fine to the coarse length scale. The model was validated based upon three

experimentally measured values: critical specific impulse, fracture patterns, and displacement at the center of the panel.

After validation, the model was used to determine a damage initiation impulse of 0.24 MPa-ms such that the panel experienced less than 1% damage. Additionally, a parametric study using the model determined that the critical specific impulse increased as the quasi-static tensile strength increased and the dissipated energy density increased. However, material designs that increase the dissipated energy density are preferred to material designs that increase the quasi-static tensile strength. This finding suggests that factors that increase dissipation, such as fiber geometry, packing, and volume fraction, are critical to improving the resistance of UHPC panels to blast loading.

The work presented here is significant for three reasons: (1) new experimental data provided an upper and lower bound to the blast resistance of UHPC panels, (2) the multiscale model simulated the experimental results using readily available properties and information regarding mesostructure attributes at two different length scales, and (3) by incorporating information from multiple length scales, the multiscale model can facilitate the design of UHPC materials to resist blast loading in ways not accessible using single length scale models.

## Acknowledgments

This work was sponsored by the Department of Homeland Security, Science and Technology Directorate, Infrastructure Protection and Disaster Management Division: Mila Kennett, Program Manager. The research was performed under the direction of Dr. Beverly P. DiPaolo, Engineer Research and Development Center (ERDC), U.S. Army Corps of Engineers (USACE). Permission to publish was granted by the Director, Geotechnical and Structures Laboratory, ERDC. Approved for public release; distribution is unlimited.

The authors gratefully acknowledge the work of Michael Mann, Jason Morson, Byron Sherwin, Kevin Taylor, Kirk Walker, and Zach Wilson, who prepared the UHPC panels at ERDC; Carolyn Johnson, Jesse Blalack, Jason Morson, Joseph Quimby, and Kirk Walker, who performed the physical testing at ERDC; and Dan Wilson, who performed the mechanical testing on the UHPC cylindrical specimens at ERDC.

## References

- [1] Naaman AE, Wille K. The path to ultra-high performance fiber reinforced concrete (UHP-FRC): five decades of progress. In: Schmidt M, Fehling E, Glotzbach C, Fröhlich S, Piotrowski S, editors. Proceedings of HiPerMat 2012 3rd international symposium on UHPC and nanotechnology for high performance construction materials. Germany: Kassel University Press; 2012. pp. 3–16.
- [2] Richard P, Cheyrez M, Roux N. Metal fiber concrete compositions for molding concrete elements, elements obtained and curing process, U.S. Patent 5,503,670, April 2, 1996.
- [3] Bache HH. Densified cement ultrafine particle-based materials. CBL Report No. 40. Denmark: Aalborg Portland; 1981. p. 1–35.
- [4] Rebentrost M, Wight G. Investigation of UHPFRC slabs under blast loads. In: Toutlemonde F, Resplendino J, editors. Proceedings of designing and building with UHPFRC: state-of-the-art, designing and building with UHPFRC. Mar-selle, France: Wiley; 2009. pp. 363–76.
- [5] Wu C, Oehlers DJ, Rebentrost M, Leach J, Whittaker AS. Blast testing of ultrahigh performance fibre and FRP-retrofitted concrete slabs. Eng Struct 2009;31(9):2060–9.
- [6] Schleyer GK, Barnett SJ, Millard SG, Wight G. Modelling the response of UHPFRC panels to explosive loading. In: Jones N, Brebbia CA, Mander U, editors. Structures under shock and impact XI. England: Wessex Institute of Technology; 2010. pp. 173–84.
- [7] Biggs JM. Introduction to structural dynamics. New York, NY: McGraw-Hill; 1964. p. 199–233.
- [8] Zhou XQ, Kuznetsov VA, Hao H, Waschl J. Numerical prediction of concrete slab response to blast loading. Int J Impact Eng 2008;35(10):1186–200.
- [9] Anon-Hardwire. Hardwire 3x2\_cord\_US. Pocomoke, MD: HardwireLLC; 2012. p. 1.
- [10] Wang J-AJ, Mattus CH, Ren F. Basic research on the materials characterization of ultra-high performance concretes: impact and penetration resistance aspects - part I. FY09 Final Report. Oak Ridge, TN: Oak Ridge National Laboratories; 2010. pp. 1–90.
- [11] DiPaolo BP, Johnson CF, Green BH, Hart WS, Magee RE, Robbins BA. Structured-materials (*Stuc'd*Mats) design concept and its application for protective structures panels: blast and sequenced ballistic-blast testing. Vicksburg, MS: U.S. Army Engineer Research and Development Center; 2012. p. 21–45. ERDC/GSL TR-12.
- [12] Bolander JE, Saito S. Discrete modeling of short-fiber reinforcement in cementitious composites. Adv Cem Based Mater 1997;6:76–86.
- [13] Bolander JE, Choi S, Duddukuri SR. Fracture of fiber-reinforced cement composites: effects of fiber dispersion. Int J Fract 2009;154(1–2):73–86.
- [14] Kim DJ, El-Tawil S, Naaman AE. Rate-dependent tensile behavior of high performance fiber reinforced cementitious composites. Mater Struct 2009;42(3):399–414.
- [15] Li VC, Wang Y, Backer S. Effect of inclining angle, bundling and surface treatment on synthetic fibre pull-out from a cement matrix. Composites 1990;21(2):132–40.
- [16] Gopalaratnam VS, Shah SP. Tensile failure of steel fiber-reinforced mortar. J Eng Mech 1987;113(5):635–52.
- [17] CEB-FIP. CEB-FIP model code 1990. London, UK: Thomas Telford; 1998. p. 39.
- [18] Anon-Lafarge. Ductal BS1000 product data sheet. France: LaFarge; 2010. p. 1–2.
- [19] Shannag MJ, Brincker R, Hansen W. Pullout behavior of steel fibers from cement-based composites. Cem Conc Res 1997;27(6):925–36.
- [20] Chan Y-W, Chu S-H. Effect of silica fume on steel fiber bond characteristics in reactive powder concrete. Cem Concr Res 2004;34(7):1167–72.
- [21] Park SH, Kim DJ, Ryu GS, Koh KT. Effect of adding micro fibers on the pullout behavior of high strength steel fibers in UHPC matrix. In: Schmidt M, Fehling E, Glotzbach C, Fröhlich S, Piotrowski S, editors. Proceedings of HiPerMat 2012 3rd international symposium on UHPC and nanotechnology for high performance construction materials. Germany: Kassel University Press; 2012. pp. 541–8.
- [22] Orange G, Acker P, Vernet C. A new generation of UHP concrete: Ductal(R) damage resistance and micromechanical analysis. In: Reinhardt HW, Naaman AE, editors. Proceedings PRO6: international RILEM conference on high performance fiber reinforced cement composites (HPFRCC 3). France: RILEM; 1999. pp. 101–10.
- [23] Anonymous. Abaqus v6.10 Theory manual. Providence, RI: Dassault Systemes; 2010.
- [24] Drucker DC, Prager W. Soil mechanics and plastic analysis or limit design. Quart Appl Math 1952;10:157–65.
- [25] Park SW, Xia Q, Zhou M. Dynamic behavior of concrete at high strain rates and pressures: II. numerical simulation. Int J Impact Eng 2001;25(9):887–910.
- [26] Johnson GR, Cook WH. A constitutive model and data for metals subjected to large strains, high strain rates and high temperatures. In: Proceedings of the 7th international symposium on ballistics. The Hague, The Netherlands: American Defense Preparedness Association; 1983. pp. 541–7.
- [27] Baltay P, Gjelsvik A. Coefficient of friction for steel on concrete at high normal stress. J Mat Civ Eng 1990;2(1):46–9.